



**9th International Conference
on
Wind Turbine Noise
Remote from Europe — 18th to 21st May 2021**

Identifying The Flap Side-Edge Noise Contribution Of A Wind Turbine Blade Section With An Adaptive Trailing-Edge

A. Suryadi¹, C. Jätz², J.R. Seume² and M. Herr¹

**¹ German Aerospace Center, Institute of Aerodynamics and Flow Technology.
Lilienthalplatz 7, 38108 Braunschweig, Germany**

² ForWind and Leibniz University Hannover, Institute of Turbomachinery and Fluid Dynamics. An der Universität 1, 30823 Garbsen, Germany

Summary

Active trailing-edge technology is a promising application for localized load alleviation of large-diameter wind turbine rotors, accomplished using one or more control surfaces in the rotor blade's outer region. This work focuses on identifying noise contributions from the flap side-edge and the trailing edge in a laboratory condition. Measurements were conducted in the Acoustic Wind tunnel Braunschweig (AWB) at the German Aerospace Center's (DLR) Braunschweig site. The small-scale model has a span of 1200 mm and a chord of 300 mm. The control surface, a plain flap, has a span of 400 mm and a chord length of 90 mm. Far-field noise was measured using a phased-microphone array for various flow speeds, angles of attack and flap deflection angles. For sound source identification, two noise reduction *addons* were installed interchangeably: trailing-edge brush and flap side-edge porous foam. Analysis of the far-field noise reveals that, while changes to the flap deflection angle alter the far-field noise spectra, the trailing-edge noise remains the predominant noise source at deflection angles -5° and 5° . No additional noise level was observed from the flap side-edge within the measurable frequency range at these angles. The flap side-edge noise has an increased role for frequency larger than 2 kHz for the larger flap deflection angles of -10° and 10° . Furthermore, numerical reproduction of the results will also be presented using the FMCAS (Fast Multipole Code for Acoustic Shielding) toolchain developed at DLR.

1. Introduction

The trend in the wind energy industry is towards larger rotor blades to produce more electricity from a single turbine. Larger rotors will experience stronger and more dynamic loads due to the fluctuating and heterogeneous wind field. Hence, there is an interest in locally distributed aerodynamic control systems. Pitch control is one strategy of load alleviation to maintain the blade's angle of attack, so that its load can be kept, on average, constant. With a larger blade, local changes to the load are preferable. One strategy uses active trailing-edges, such devices can be a flap or an aileron. Either way, it modifies the lift coefficient by changing the camber of the profile.

Load alleviation is studied in the framework of project *SmartBlades 2.0*, which has the overall goal of demonstrating the practical applications of technologies for rotor blade control and val-

identifying suitable innovative and manufacturing methods. One of the technologies studied in the project is load alleviation using an active trailing-edge. This is presently accomplished using a plain flap on the outboard section ($0.825 \leq R/R \leq 0.9$) of the rotor blade from the conceptual wind turbine IWES IWT-7.5-164 [1] which has a blade length of $R=80$ m. The present plain flap installation means that when active, the trailing edge is no longer a continuous line and a new edge is exposed from the flap's side. The newly exposed edges have the potential to be a noise radiator.

Flap side-edge noise has been covered extensively in the aeronautical industry [2, 3, 4, 5, 6, 7, 8, 9, 10, 11, 12], whereas in the wind energy industry, the study focuses on the implementation and the aerodynamic effect of flap on wind turbine rotor blades [13, 14, 15, 16, 17]. In aeronautics the flap is implemented differently than in the wind energy industry. Namely, in the types of flap used, Fowler flap in aeronautics and plain flap in wind energy, and in the degree of flap deflection, $\delta_f > 20^\circ$ in aeronautics [9, 18] and $|\delta_f| \leq 10^\circ$ in wind energy [15]. To the authors' knowledge the noise radiation from the flap side-edge of a rotor blade has not been extensively explored. A few reasons for this state-of-the-art are: (i) the desired implementation is one that maintains a continuous trailing edge and (ii) the flap deflection angle is small enough that flap side-edge noise is assumed negligible.

In this study, a small-scale test was conducted in the Acoustic Wind tunnel Braunschweig located at the German Aerospace Center's (DLR) Braunschweig site to measure and rank the flap side-edge noise compared to the trailing-edge noise. A segment of the rotor blade, which has the DU08-W-180 profile shape, is scaled down as a 1200 mm span and a 300 mm chord wind tunnel model. The model's shape and chord length are constant. The plain flap has a 400 mm span and a 90 mm chord, capable of being deflected negatively (upwards, towards the suction side) and positively (downwards, towards the pressure side). As a comparison, the small scale wind tunnel model has a chord-based Reynolds number of 0.95×10^6 , whereas a similar section in the full-scale rotor has 12.6×10^6 .

The paper is structured as follows: first, the experimental setup is detailed, followed by an explanation of the identification of sound sources using noise reduction materials. The results are presented and discussed in the two following sections, and finally, a conclusion from the study is drawn.

2. Experimental Setup

2.1. Wind Tunnel Facility

The Acoustic Wind tunnel Braunschweig (AWB) is a Göttingen type, open section, acoustically insulated wind tunnel. It is capable of producing a maximum wind speed of 65 m/s with 0.3% turbulence intensity [19]. The freestream is introduced into the open section from a 0.8 m wide and 1.2 m high nozzle.

The wind tunnel's test section and the blade model installed within are shown in Figure 1. A phased-microphone array with 96, 1/2-inch LinearX microphones was used to measure the noise radiated from the blade model. The measurement has a sampling rate 65 kHz and a sampling time of 20 s. Noise mapping was performed using the CLEAN-SC algorithm, which allows for separating different noise sources by defining specific regions of interest on the model [20]. The algorithm provides a margin of approximately ± 2 dB within a 95% confidence interval. Measurements were conducted with the phased-microphone array alternately facing the blade model's suction and pressure sides. Because there is no unexpected difference from both sides, the upcoming analysis will present only the suction side.

2.2. Blade Section Model

The blade section model with DU08-W-180 profile was installed vertically in the wind tunnel section, as shown in Figure 1. The model has a span of 1200 mm and a chord length of 300 mm. The plain flap was installed in the mid-span section of the model. The flap's span is 400 mm, and its chord length is 90 mm, see also figure 2. A motor is attached to the outside of the model to drive the flap. During the measurements, the flap angle is fixed, and the flap is only driven

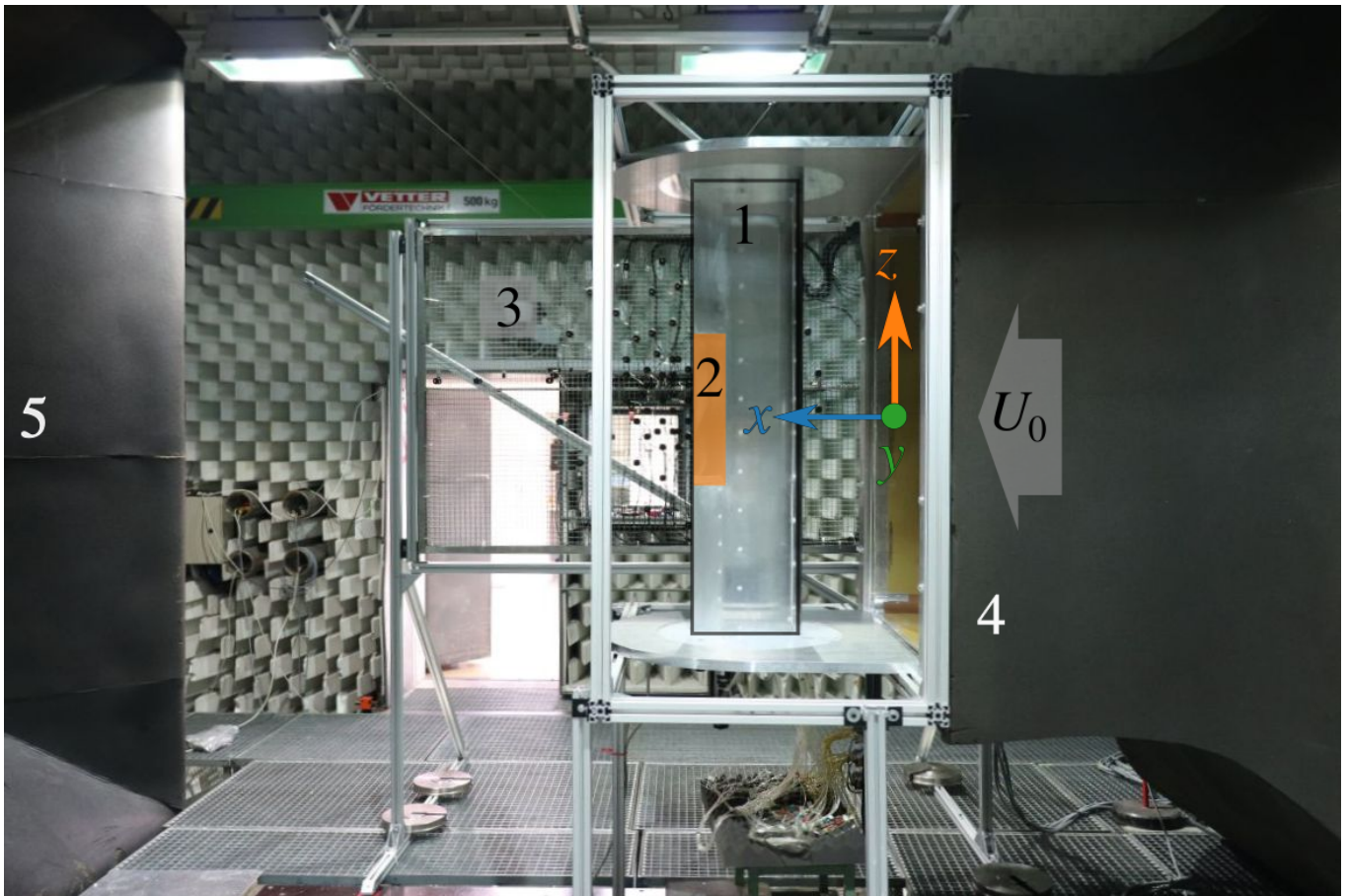


Figure 1: The blade section model, (1), with a plain flap, (2), and the phased-microphone array, (3), inside the AWB test section. Also shown are the wind tunnel nozzle, (4), and collector, (5).

in-between measurements.

By design, wind turbine rotors have a thick blunt trailing edge. The chord-length based scaling down of the model results in a trailing edge thickness of 2 mm leading to bluntness noise in the laboratory scale. Hence, the trailing edge is further reduced to 0.3 mm, akin to a sharp trailing edge.

For motion with minimal friction, the gap between the flap side-edge and the model's side-edge is approximately 0.2 mm. This gap is left untreated. The gap in the span-wise direction between of the flap and the model is sealed using aluminum tape, creating a smooth and continuous transition between both parts and prevents a cross-flow from the pressure side to the suction side, eliminating potential acoustic noise source.

The blade section model is equipped with two sets of static pressure ports. The first set is along the mid-span for monitoring the pressure coefficients when the flap is deflected. The second set is 400 mm away from the mid-span for monitoring the reference, zero-flap-deflection pressure coefficients. The boundary layer was tripped using a 0.205 mm high zig-zag trip on the suction side at the $x/c = 0.05$ and on the pressure side at the $x/c = 0.10$ to emulate high Reynolds number transition location.

2.3. Experimental Parameters

The angular parameters shown in Table 1 were measured in the wind tunnel at windspeeds of $U_0 = 40$ m/s, 50 m/s, and 60 m/s. The angle of attack α_g signifies the geometric angle as set in the wind tunnel. The equivalent aerodynamic angle of attack is α_a . For $\alpha_g = 13^\circ$, the flap deflection angles δ_f is limited because the combination of the large angle of attack and positive flap deflection the wake is deflected outside of the flow collector region.

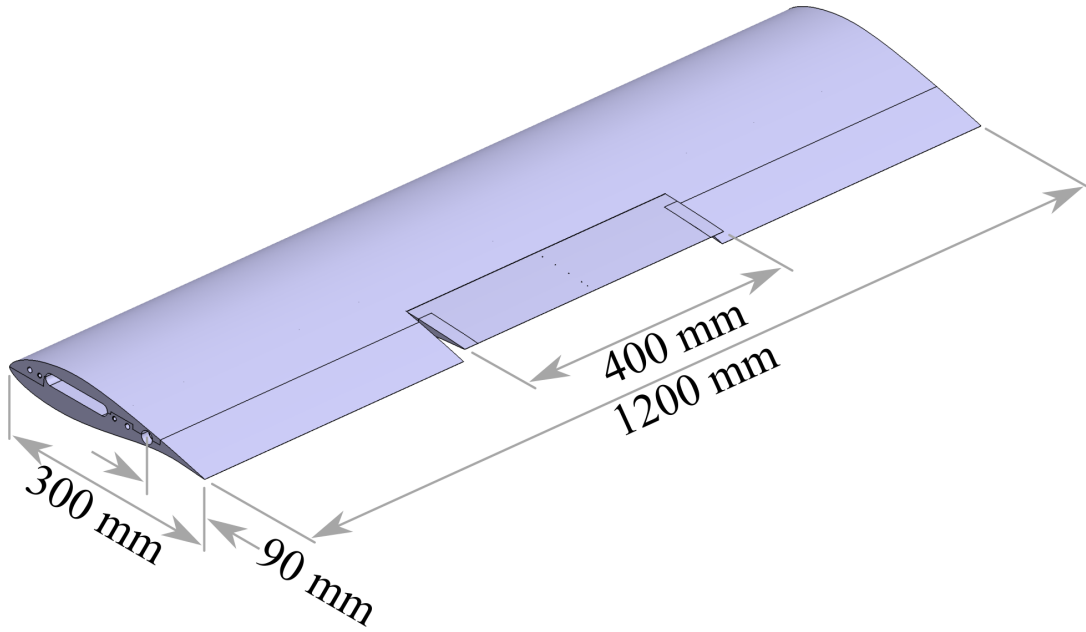


Figure 2: The blade section model DU-08-W-180 with flap set at $\delta_f = -10^\circ$.

3. Numerical Setup

In addition to the experiments in the wind tunnel, numerical simulations were conducted. Steady RANS simulations provide a detailed insight into the flow field and are the input for the numerical aeroacoustic analysis. Due to symmetry, the size of the model and the required high mesh resolution, the numerical domain comprises only a side-edge and extends 150 mm span-wise in both directions. The far field extends to 100 chord lengths.

The mesh is block structured. The topology was carefully designed so that the cells between all blocks in the side-edge region match conformally. This eliminates the need for an interpolating interface, eliminating spurious errors in the region of interest. The initial cell height at the blade surface was chosen to achieve a y^+ -value of less than 1. This allows the application of low-Reynolds number turbulence models for a more accurate representation of the boundary layer. The growth ratio in wall-normal direction is 1.1. The cell resolution in the side-edge region was increased according to the requirements for the aeroacoustic analysis. Overall, the mesh contains about $30 \cdot 10^6$ cells.

The simulations were carried out using the coupled implicit solver with a second-order discretization in Star CCM+. For closure of the RANS equations, the $k-\omega$ SST turbulence model was selected as this model provides the required flow field quantities for the subsequent aeroacoustic analysis. In order to capture the forced transition by the applied tripping in the wind tunnel, a turbulent suppression approach was selected. Here, the turbulence model is deactivated upstream of the tripping location, resulting in a laminar flow. Downstream of the tripping location, a turbulent boundary layer develops.

The convergence of the simulations was verified by the decrease of the average and maximum residuals. Additionally, lift and drag coefficients were monitored as they converged to constant values.

Table 1: Angle of attack α_g , α_a and flap deflection angle δ_f .

$\alpha_g, ^\circ$	$\alpha_a, ^\circ$	$\delta_f, ^\circ$
5	0	-10, -5, -4, ... 4, 5, 10
7	3	-10, -5, -4, ... 4, 5, 10
13	6	-10, -5, -4, ... 0

4. Noise Reduction Technologies

Noise mitigating addons were used to inhibit selective noise radiation and to identify the noise source from a blade section of the present scale. For example, to identify the contribution of the flap side-edge noise, noise-reducing brush was added to the trailing edge. Conversely, to identify the contribution of the trailing-edge noise, the flap side-edge is substituted with a porous copy.

4.1. Trailing-Edge Brush

The trailing-edge brush [21] consists of elastic needles that are 0.4 mm in diameter. The brush is one layer thick and with a density of 250 needles/m along the span and a length of 60 mm. It was installed on the trailing edge's pressure side using a double-sided adhesive tape. Further structural support is provided by an aluminum tape, which also allows for a smooth transition of the boundary layer from the model's surface to the brush. The installed trailing-edge brush is shown in Figure 3(a).

4.2. Porous Side-Edges

Two porous copies of the flap side-edges were manufactured using an electrical discharge machining process. This process allows for shaping the porous foam to the shape of the flap side-edge. These substitutes, when installed, will provide a porous side-edge with a depth of 20 mm. The porous materials are PA 80-110 and PA 120-150, which were supplied by Exxentis AG. The properties of the porous materials are provided in Table 2 and the two materials are shown in Figure 3(b) and (c). The porosity, the ratio of open volume to the total volume, and the specific resistance, the pressure loss of a flow passing the material per unit velocity were measured by the Institute for Materials, TU Braunschweig. These materials were extensively investigated for trailing-edge noise reduction [22, 23].

Table 2: Porous material properties

Specimen	Nominal pore size [μm]	Porosity [%]	Specific resistance [Ns/m^3]
PA 80-110	80–110	56	540
PA 120-150	120–150	57	245

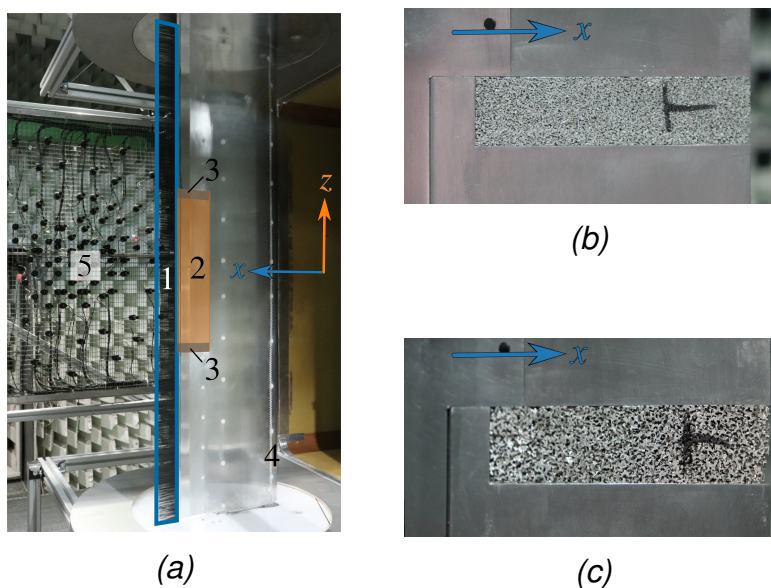


Figure 3: (a) The blade section model viewed from the pressure side with the trailing-edge brush (1), the flap (2), the exchangeable flap side-edges (3), the boundary layer tripping (4) and the phased-microphone array (5). Porous flap side-edges, (b) PA80-110 and (c) PA120-150, viewed from the suction side of the blade section model.

5. Results

5.1. Pressure Coefficients

The measured pressure coefficients are shown in Figure 4 for all measured angles of attack. For brevity only $\delta_f = -10^\circ, -5^\circ, 0^\circ, 5^\circ$ and 10° are shown for the pressure coefficients and the sound pressure levels. The margin of error for the measured pressure coefficient is ± 0.026 within a 95% confidence interval.

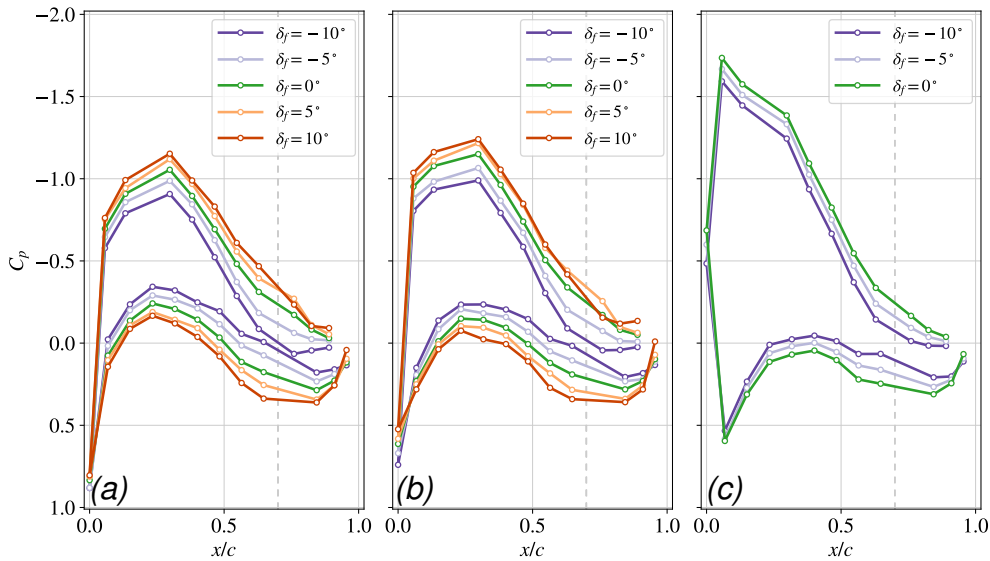


Figure 4: Experimental pressure coefficients at $\delta_f = 0^\circ$ and $|\delta_f| = 5^\circ$ and 10° , (a) $\alpha_g = 5^\circ$, (b) $\alpha_g = 7^\circ$, and (c) $\alpha_g = 13^\circ$.

5.2. Relevant Frequency Range

The *exterior* noise, anything other than the model's self-noise, was measured with the same tools and relevant measurement parameters without the blade section model installed to identify the meaningful frequency range. For this purpose, the region of interest defined in CLEAN-SC for the analysis of trailing-edge noise is an area with a span width of $b_g = 0.7$ m and streamwise length of $c_g = 0.2$ m. For the analysis of exterior noise, the region of interest encompasses the full-span of the blade section model, $b_g = 1.2$ m and from the AWB nozzle to 1.2 m downstream.

The sound maps of selected one-third octave center frequencies are shown in figure 5(a) the exterior noise and in figure 5(b) for the trailing-edge noise. The sound maps' red line highlights the sound contour where $\max(L_{p,1/3}) - 3$ dB. The trailing edge is located at $x = 0.55$ m, and at $x = 0.8$ m is the location of the edge of the top and bottom support walls (see figure 1). The sound maps in figure 5(a) show that the support walls' edges radiate sound that is louder than the trailing-edge noise at $f_c = 5000$ Hz, and it remains louder for center frequencies higher than 5000 Hz. Despite this, the sound pressure levels at $f_c > 5000$ Hz scale well with the U_0^5 trailing-edge noise, as shown in the next section, because of the decreasing acoustic wavelength. Hence, due to excess noise from the edges of the support walls, the figures involving sound pressure level will exclude the spectral level at $f_c = 5000$ Hz.

5.3. Reference Trailing-Edge Noise

The one-third octave sound pressure level is shown in figure 6 for $\delta_f = 0^\circ$ with and without the trailing-edge noise U_0^5 scaling law. To focus on the trailing-edge noise, the region of interest encompasses the trailing edge with $b_g = 0.7$ m and $c_g = 0.2$ m. The characteristic lengthscale chosen for the scaling law is the suction side boundary layer displacement thickness δ_1 at the trailing edge, and the characteristic velocity is the freestream velocity U_0 . All characteristic values are given for $\delta_f = 0^\circ$. Together, they scale the low to medium frequency well [24]. The displacement thicknesses were calculated using XFOIL [25] and are presented in Table 3.

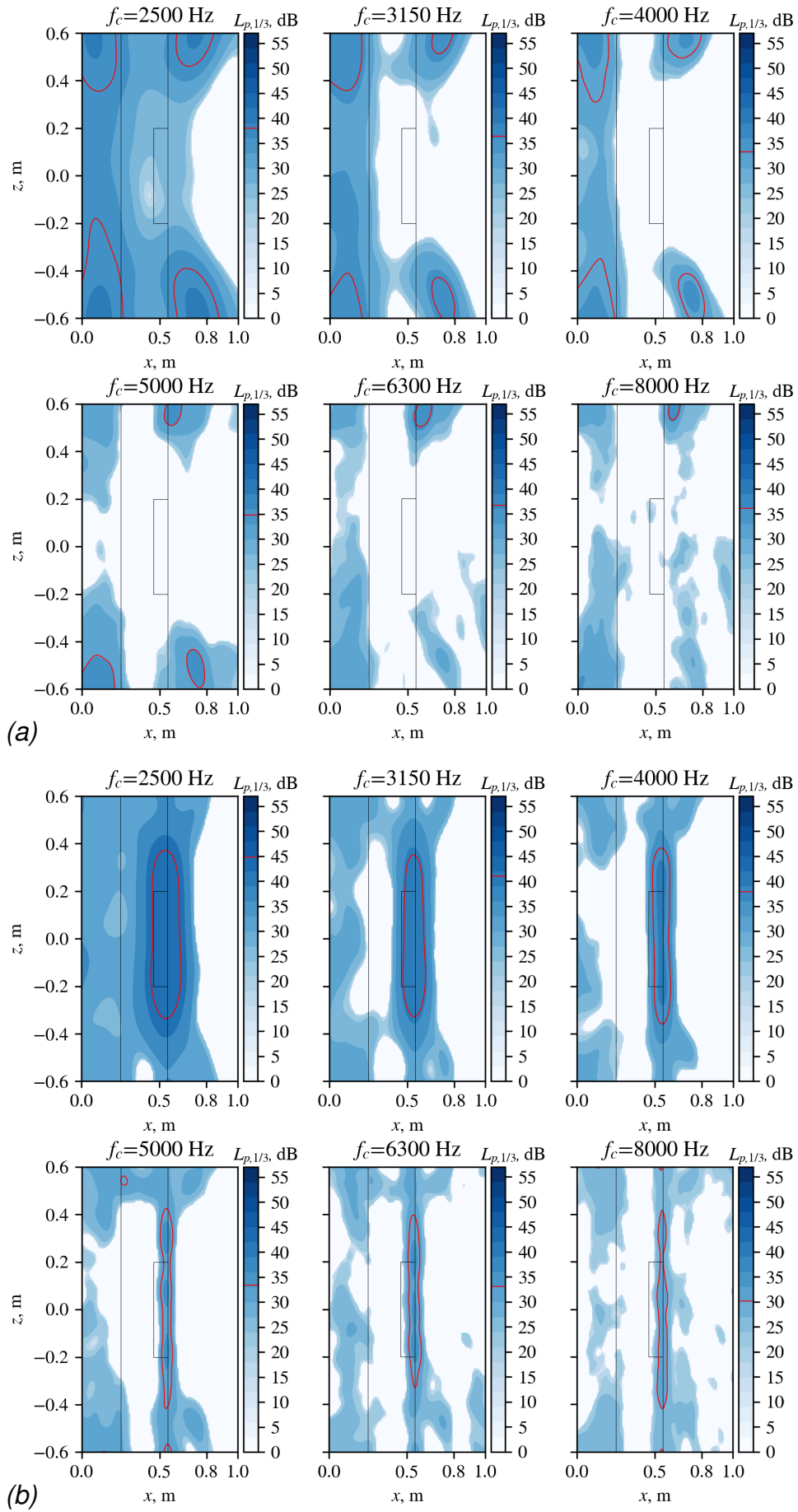


Figure 5: Sound maps with $U_0 = 50$ m/s (a) exterior noise and (b) trailing-edge noise $\alpha_g = 5^\circ$, and $\delta_f = 0^\circ$. The sound contour where $\max(L_{p,1/3}) - 3$ dB is highlighted by the red line.

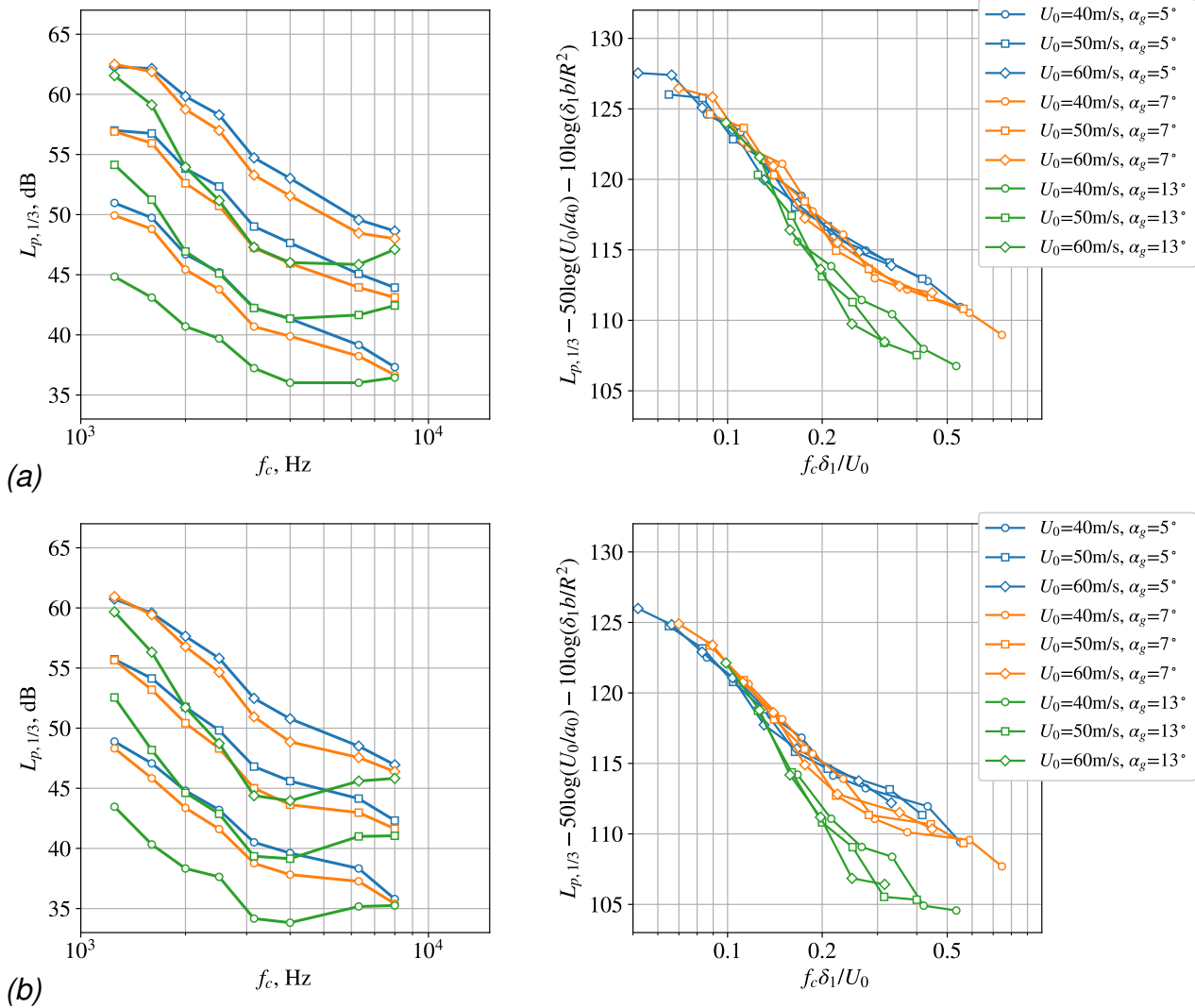


Figure 6: Unscaled and scaled sound pressure level of trailing-edge noise measured with the phased-microphone array (a) facing the suction-side and (b) facing the pressure-side of blade section model.

It is apparent, from figure 6, the sound pressure level is lower over the measured frequency range for the same U_0 and increasing α_g . This observation can be explained by the increase of boundary-layer thickness and the adverse pressure gradient. As a reminder, $f_c = 5000$ Hz is dropped in the spectra as described in the previous section. After scaling, it was found that the sound pressure levels are self-similar for $f_c < 2000$ Hz, but the self-similar spectra diverge according to α_g at higher frequency as a result of increasingly adverse pressure gradient [26]. Furthermore, at $\alpha_g = 13^\circ$, the spectral level increases for $f_c > 5000$ Hz for the non-scaled spectra, which is atypical for trailing-edge noise. Hence, to avoid confusion, the scaled spectra of $\alpha_g = 13^\circ$ are limited to $f_c \leq 4000$ Hz.

Table 3: Suction side boundary layer displacement thickness δ_1 computed at the trailing edge.

U_0 , m/s	δ_1/c		
	$\alpha_g = 5^\circ$	$\alpha_g = 7^\circ$	$\alpha_g = 13^\circ$
40	0.009169	0.012441	0.017808
50	0.008675	0.011728	0.016660
60	0.008299	0.011188	0.015802
150	0.006014	0.008434	0.012626

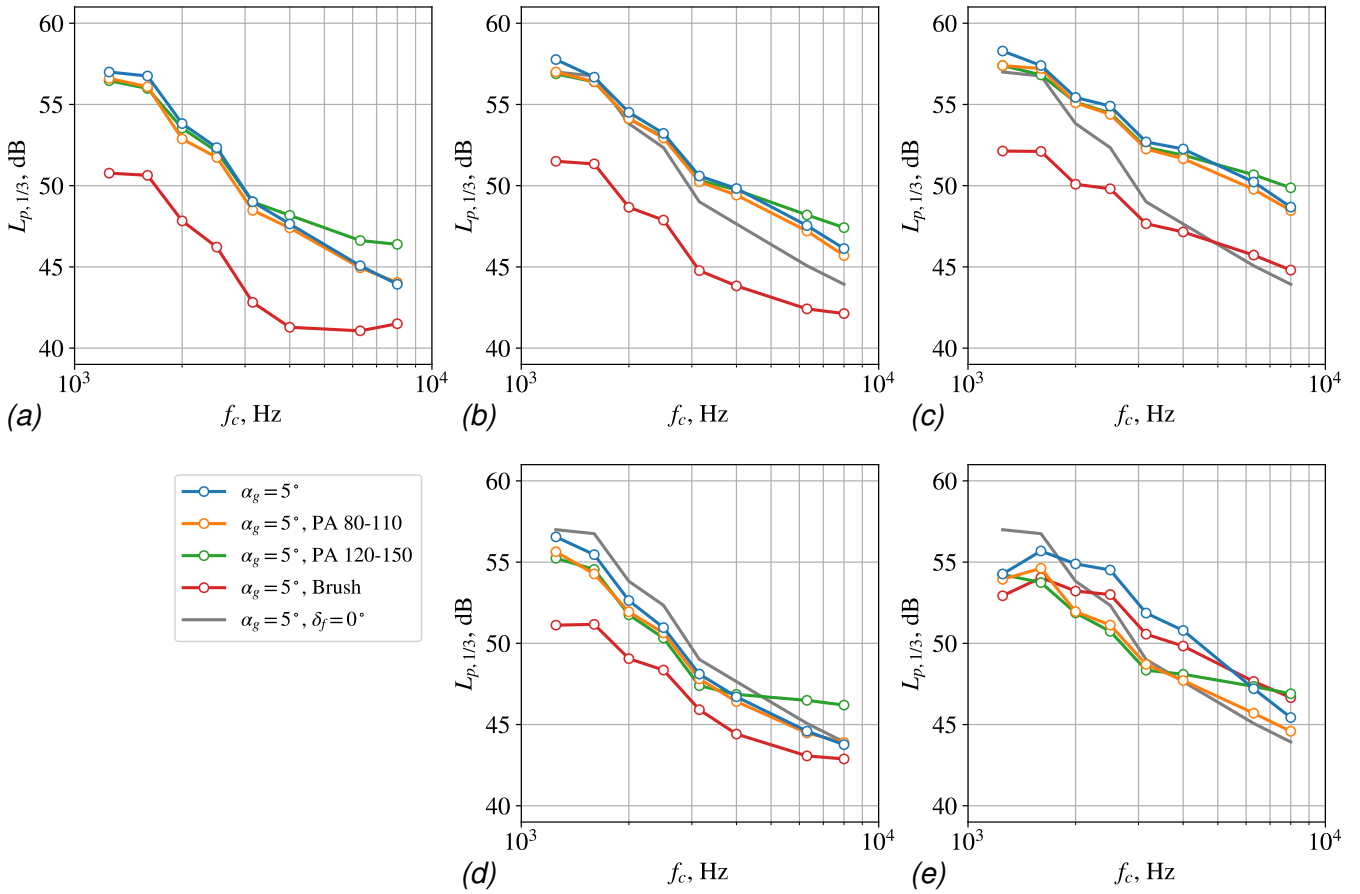


Figure 7: The farfield sound pressure level, $b_g = 0.7$ m. (a) $\delta_f = 0^\circ$, (b) $\delta_f = -5^\circ$, (c) $\delta_f = -10^\circ$, (d) $\delta_f = 5^\circ$, (e) $\delta_f = 10^\circ$.

5.4. Effect of Edge Noise Reduction Technologies

The flap side-edge porous substitutes were installed and measured in the same way as a solid flap side-edge to localize the noise source. The region of interest is the same one used when investigating trailing edge scaling. The resulting sound pressure levels for porous flap side-edge, trailing-edge brush, and solid flap side-edge are shown in figure 7.

5.4.1 Trailing-Edge Noise

The $\delta_f = 0^\circ$ configuration in figure 7(a) has the porous material affecting only 1/30 of the span length of the model's trailing edge. Hence, the porous material has little effect on the trailing-edge noise reduction. Noise increase was measured for PA120-150 side-edge at $f_c > 4000$ Hz because of the increased surface roughness [27]. In contrast, the trailing-edge brush was applied to the full span of the trailing edge. Hence, the porous material's effectiveness for reducing the trailing-edge noise is considerably lower than that of the brush.

The flap-up configuration of $\delta_f = -5^\circ$ in figure 7(b) gradually increases the sound pressure level at higher frequencies compared to the non-deflected flap configuration. Whereas the flap-down configuration results in a broadband reduction in sound pressure level. This alteration of the sound pressure level can be attributed to the local boundary layer's change above the flap's surface. For the $\pm 5^\circ$ change of flap angle, the sound pressure levels for both porous flap side-edges are similar to those of the solid flap side-edge. Similar to the non-deflected flap case, the trailing-edge brush produces a 6 dB reduction in sound pressure level. Hence, for the $\pm 5^\circ$ flap angle deflection, the flap side-edge noise is not as apparent as the trailing-edge noise in the relevant frequency range.

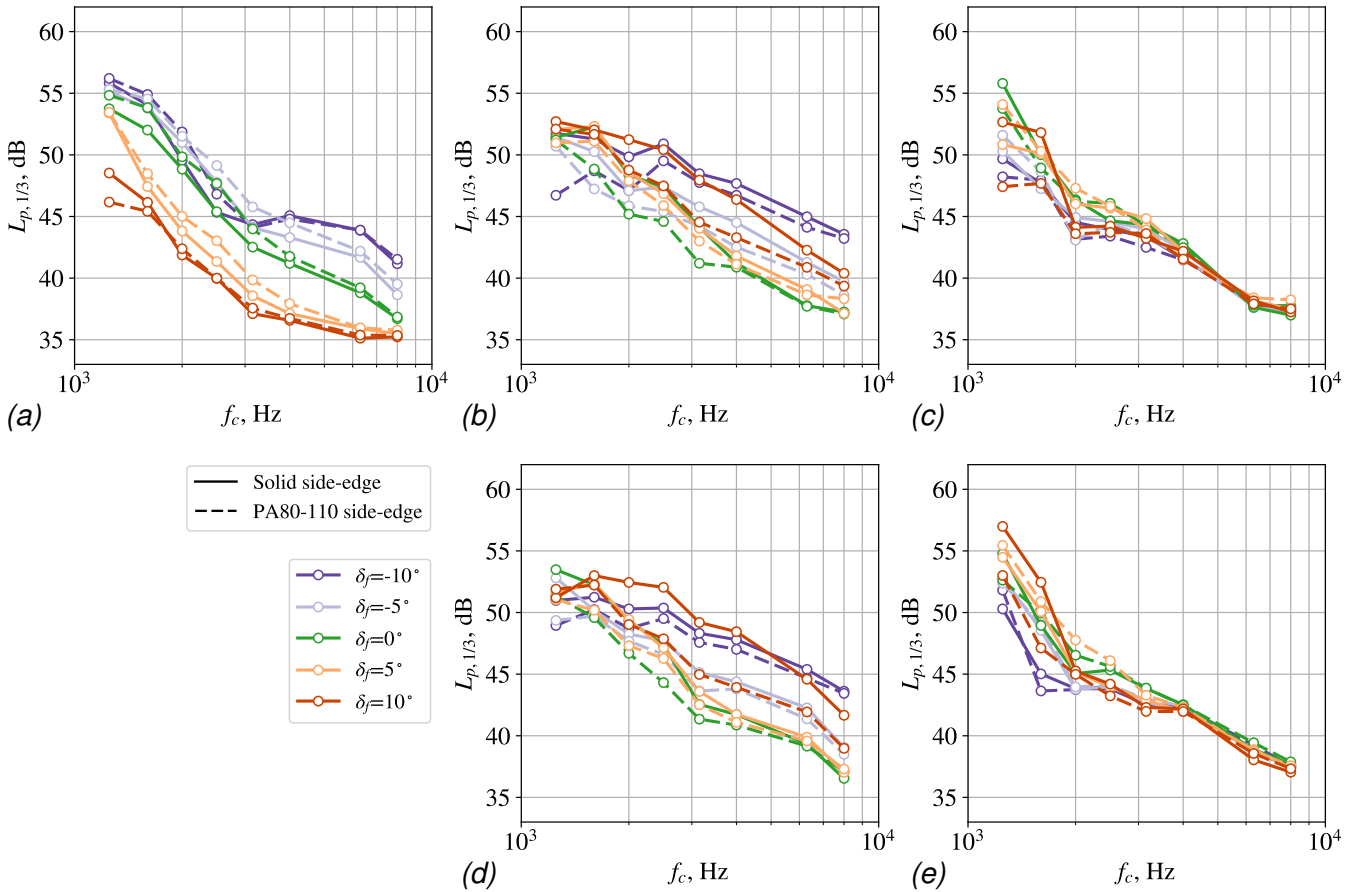


Figure 8: Contributions to the farfield sound pressure level according to the narrow spanwise sections centered at z_c with $b_g = 0.2$ m and $\alpha_g = 5^\circ$. (a) $z_c = 0$ m, (b) $z_c = -0.2$ m, (c) $z_c = -0.4$ m, (d) $z_c = 0.2$ m, (e) $z_c = 0.4$ m.

5.4.2 Flap Side-Edge Noise

The flap-up configuration $\delta_f = -10^\circ$ in figure 7(c) is fundamentally different than the flap-down one $\delta_f = 10^\circ$ in figure 7(e). For $\delta_f = -10^\circ$, the porous flap side-edge does not alter the sound pressure level, whereas for $\delta_f = 10^\circ$ both porous flap side-edges and trailing-edge brush alter the sound pressure level compared to the solid flap side-edge.

In a first look, it appears that the flap side-edge noise is not relevant for $\delta_f = -10^\circ$. However, this outlook could result from the porous material only applied on the flap's side and not on the model's side. The spectra contributed by the narrow strips of the model's trailing edge, $b_g = 0.2$ m, centered at z_c are shown in figure 8, which for brevity shows only the solid flap side-edge and the PA 80-110 flap side-edge. It was confirmed that the sum of sound pressure levels of the narrow sections is equal to the sound pressure level of a region with a span equal to the sum of the span of the narrow sections. Figure 8 classifies 3 general regions of the model as detailed below:

1. The first region is around the midspan of the model, figure 8(a), where the porous flap side-edge shows little relevance. Changes to the sound pressure level in this figure are related to the value of δ_f , which changes the local boundary layer dynamics.
2. The second region encompasses the flap side-edge and shown in figure 8(b) and (d). The effect of the porous flap-side edge is most notable for $\delta_f = 10^\circ$ as depicted in figure 7. The porous flap side-edge significantly affects the sound pressure level even for $\delta_f = 0^\circ$, because the region processed by CLEAN-SC is a narrow strip focused around the flap side-edge.
3. The final region is the outboard region shown in figure 8(c) and (e). The effect of δ_f to the sound pressure level is limited to $f_c < 2000$ Hz. The effect of porous side-edge is shown only for $\delta_f = 10^\circ$. The sound pressure levels at $f_c > 2000$ Hz is only dependent to α_g .

Comparison of the flap-side edge region, figure 8(b) and (d), and the outboard region, figure 8(c) and (e), shows that the solid flap side-edge increases the localized sound pressure level for $f_c > 2000$ Hz and it is observed for $\delta_f = -10^\circ$ and 10° . However, the porous side-edge is effective in reducing flap side-edge noise only at $\delta_f = 10^\circ$. This behavior can be explained by figure 9 that shows the flap side-edge vortex for (a) $\delta_f = -5^\circ$ and (b) $\delta_f = 5^\circ$. Figure 9(a) shows that the predominant side-edge vortex develops from the side-edge of the static model, whereas figure 9(b) shows that it develops from the flap side-edge. Because the porous material is only installed on the flap side-edge, figure 9 is a compelling argument that the porous side-edge is ineffective in reducing flap side-edge noise in the flap-up configuration. The flap deflection angles of the simulated flow field are smaller than those observed in the measurement, however, we believe that the physical phenomenon explained here is retained.

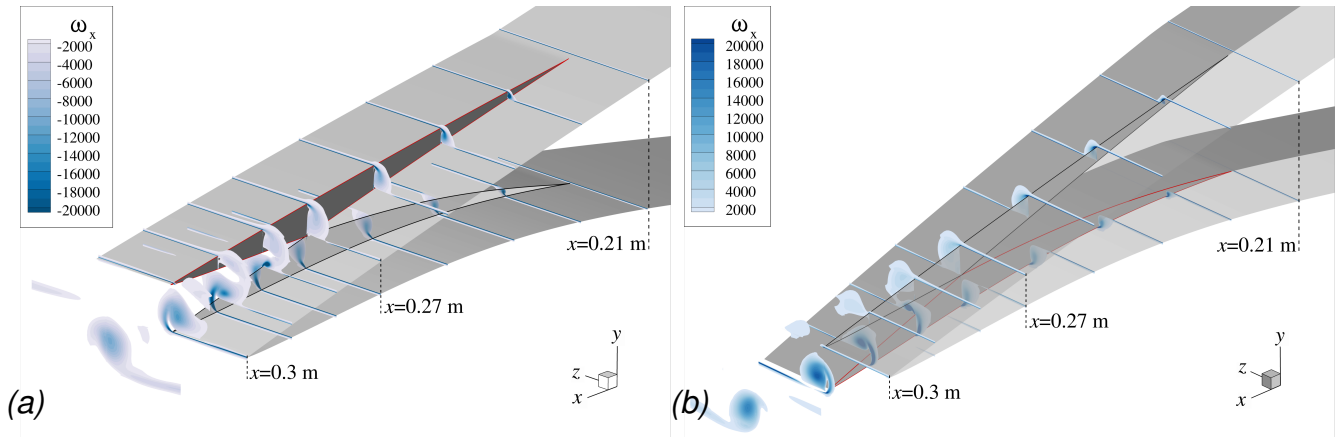


Figure 9: k - ω SST simulations of the flap side-edge vortex with $U_0 = 50$ m/s and $\alpha_a = 0^\circ$ (a) $\delta_f = -5^\circ$, (b) $\delta_f = 5^\circ$. The flap side-edge is demarked by a red line and the color contour depicts the strength of the chordwise vorticity.

6. Discussion

6.1. Noise of Active Trailing-Edge

The IWT-7.5-164 wind turbine's design angle at $R = 76$ m is 6° , which is achieved in the wind tunnel measurement at approximately $\alpha_g = 13^\circ$. However, the blade section model at the flap-down configuration at this angle of attack deflects the flow greatly. Under such conditions the wake would directly impinge on the flow-collector wall, causing blockage effects and potentially structural damage to the wind tunnel. Therefore, the reference angle of attack in the wind tunnel measurement is $\alpha_g = 7^\circ$ or equivalent to the aerodynamic angle of attack α_a of 3° .

For the present blade section model with flap, a flap deflection of $+5^\circ$ results in a change of lift equivalent to -3° change in the effective angle of attack and vice versa. The pressure coefficients and sound pressure levels of the angle of attack and flap deflection angle combination are shown in figure 10. The pressure coefficient distribution of $(\alpha_g = 5^\circ(0^\circ), \delta_f = 0^\circ)$ in figure 10(a) is altered because of the flap deflection of $\delta_f = 5^\circ$ and it is now approximately similar to pressure coefficient of the design point in figure 10(b). At $\alpha_g = 13^\circ$, the flap deflection does not alter the pressure coefficient back to the design point, notably because the pressure minimum at $\alpha_g = 13^\circ$ has moved closer to the leading edge.

The corresponding sound pressure levels for these configurations are shown in figure 10(b) without flap deflection and figure 10(c) with flap deflection. The active trailing-edge equalizes the blade model's self-noise.

Therefore, in maintaining constant lift using a plain flap, within the envelope of $\pm 3^\circ$ effective angle of attack change from the reference angle of attack, there is no noise increase, within the measured frequency range, related to the flap side-edge noise from the flap deflection of $\pm 5^\circ$.

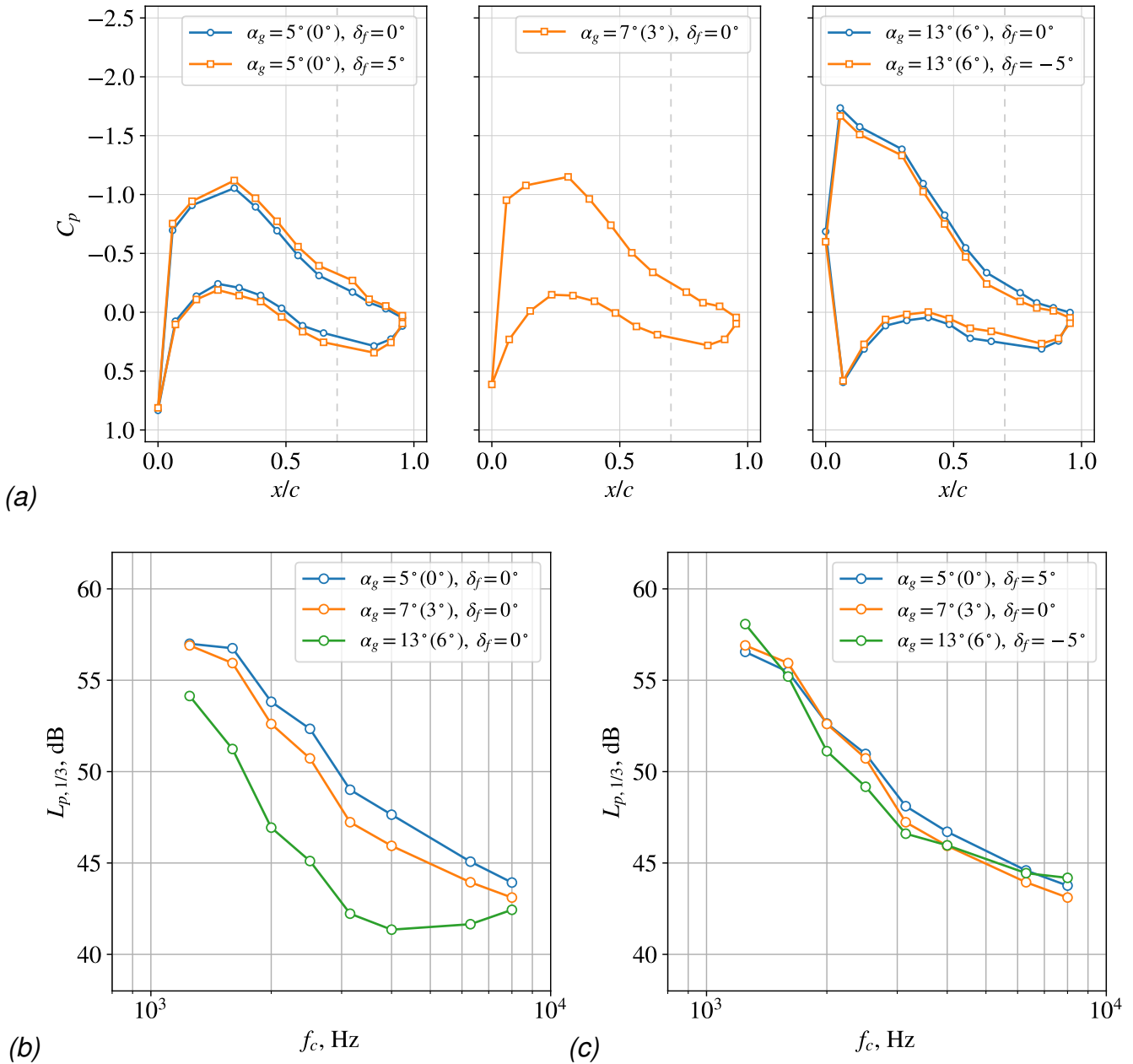


Figure 10: Pressure coefficients (a) without and with flap deflection and the one-third octave sound pressure levels (b) without flap deflection and (c) with flap deflection. The value in parentheses indicates the equivalent aerodynamic angle of attack.

6.2. FMCAS: Fast Multipole Code for Acoustic Shielding

FMCAS is a tool designed to investigate acoustic shielding but is also capable of trailing-edge noise prediction [28, 29]. FMCAS uses the reconstructed turbulent flow field of FRPM (Fast Random Particle Mesh), which is generated with input from RANS, to calculate sound radiation. The details of FMCAS is beyond the scope of this study and will be addressed in a different paper. Figure 11 shows the spectral comparison between FMCAS and the measurements. A small flow patch was used as input for producing the numerical spectrum. This patch contains the flow information around the flap side-edge and is only 64 mm wide to limit the trailing-edge noise's contribution. Hence, the numerical spectrum approximates the flap side-edge noise. The grey lines indicate the upper and lower 95% confidence levels of the simulation due to the stochastic nature of the turbulence flow field reconstruction of FRPM.

The measured spectrum shown in figure 11 is the sound pressure level of the solid flap side-edge, $L_{p,1/3, \text{solid}}$, for no-flap $\delta_f = 0^\circ$, medium-flap $|\delta_f| = 5^\circ$, and high-flap $|\delta_f| = 10^\circ$. These spectra were calculated with CLEAN-SC from a region with a span width of $b_g = 0.1$ m surround-

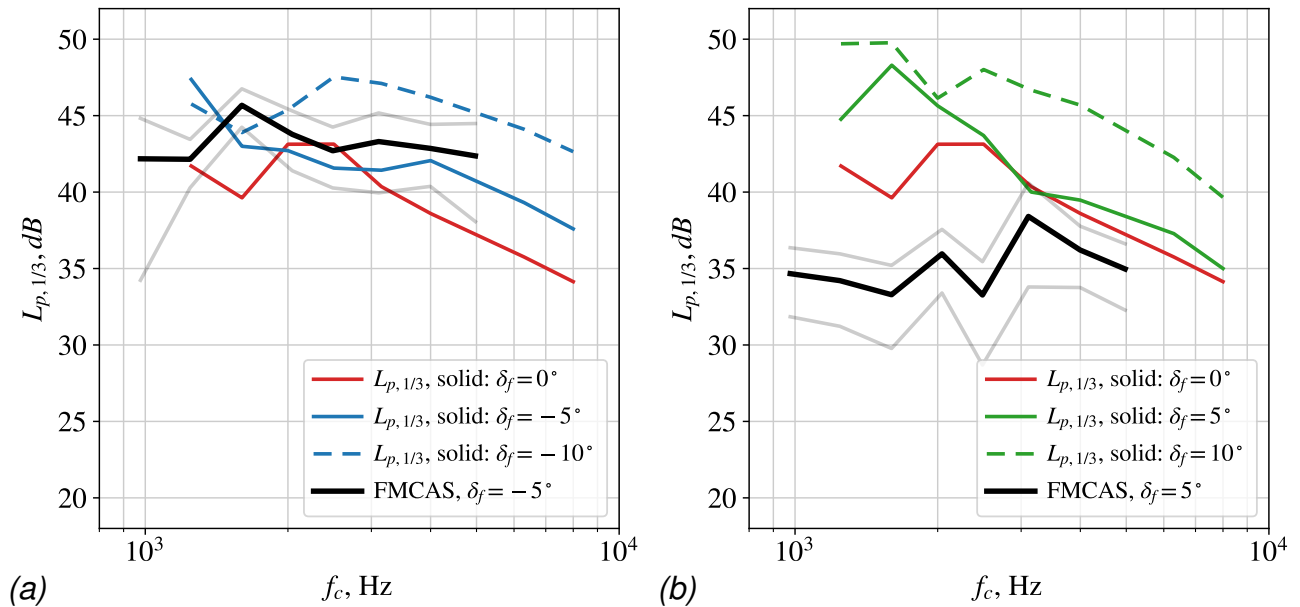


Figure 11: Comparison of the spectra from FMCAS simulation and from the experiment $U_0 = 50$ m/s and $\alpha_a = 0^\circ$ (a) flap-up and (b) flap-down.

ing the flap side-edge. The result shows that FMCAS can reproduce the flap side-edge noise spectrum for $\delta_f = -5^\circ$ in figure 11(a), but less reproducible is the spectrum for $\delta_f = 5^\circ$ in figure 11(b). The reason for the discrepancy could be due to the boundary layer thickening and also the adverse pressure gradient introduced by the flap and not captured in the numerical simulation. For example, The change of δ_f from no-flap to medium-flap in figure 11(b) shows a level increase at $1250 \leq f_c \leq 2000$ Hz. This level increase is not observed in figure 11(a).

Another feature of the measured sound pressure levels in figure 11 is that the flap side-edge noise is relevant for $f_c > 2000$ Hz at $\delta_f = \pm 10^\circ$. Whereas for $\delta_f = \pm 5^\circ$ the relevant frequency range is $f_c > 3000$ Hz. This feature is in agreement with the flap side-edge scaling in Ref. [30], which proposed that the flap side-edge noise scales with the diameter of the cross-section of the flap side-edge vortex and the local crossflow velocity.

FMCAS shows promise in predicting flap side-edge noise. The sound pressure level of $\delta_f = -5^\circ$ is well predicted, but less well for $\delta_f = 5^\circ$. Presumably, the localized flow domain used to resolve the numerical spectrum is too small to capture the acoustic effect of the flap-down configuration's thick boundary layer.

7. Conclusions

A small-scale blade section was measured in the Acoustic Wind tunnel Braunschweig to investigate the acoustic effect of implementing an active trailing-edge. The blade section has a 400 mm span wide and 90 mm chord long flap. Three freestream velocities, three angles of attack, and flap deflection angles between -10° to 10° were measured using a phased-microphone array. Because of the physical model scale, noise reduction technologies were used to minimize individual sound sources. A trailing-edge brush was implemented at the static and active trailing-edge. A narrow part of the flap side-edge is substituted with a porous material to reduce flap side-edge noise and identify the trailing-edge noise.

The measured far-field noise spectra show that the trailing-edge brush performs best at all flap deflection angles, except for the flap deflection angle of $\delta_f = 10^\circ$, where porous side-edges are more effective for noise reduction. The sound pressure level of a narrow region around the flap side-edge at $\delta_f = -10^\circ$ is higher than the rest of the trailing edge for $f_c > 2000$ Hz. However, at $\delta_f = -10^\circ$, the porous side-edge material does not reduce noise as optimally as at $\delta_f = 10^\circ$. Hence, it can be concluded that flap side-edge noise is not a relevant noise source for the small flap deflection angles between -5° and 5° .

The active trailing-edge is designed to achieve 5° flap deflection to compensate for -3° angle-of-attack change and vice-versa. Both positive and negative trailing edge deflections produce sound pressure levels comparable to the reference angle of attack within the measured frequency range. Hence, the flap side-edge noise is not a significant contributor to an active trailing-edge for the flap deflection angles in the $-5^\circ \leq \delta_f \leq 5^\circ$

Flap side-edge noise prediction was attempted using FMCAS, which shows promise in localizing the contribution of the flap side-edge noise. However, the comparison with measurements has to be undertaken carefully, as the measured spectrum combines other, more predominant noise sources.

Acknowledgement

The authors' are grateful to Jörn Tychsen (TU Braunschweig) for providing the porous foam materials. This study, part of the project SmartBlades 2.0, was funded by the German Ministry for Economic Affairs and Energy (BMWi).

References

- [1] IWES Wind Turbine IWT-7.5-164. Rev 4. Technical report, Fraunhofer IWES.
- [2] Jay C. Hardin. Noise radiation from the side edges of flaps. *AIAA Journal*, 18(5):549–552, May 1980.
- [3] M.S. Howe. On the generation of side-edge flap noise. *Journal of Sound and Vibration*, 80(4):555–573, February 1982.
- [4] R. Sen. Local dynamics and acoustics in a simple 2D model of airfoil lateral-edge noise. In *Aeroacoustics Conference*, State College, PA, U.S.A., May 1996. American Institute of Aeronautics and Astronautics.
- [5] Jay C. Hardin and James E. Martin. Flap Side-Edge Noise: Acoustic Analysis of Sen's Model. *AIAA Journal*, 35(5):810–815, May 1997.
- [6] C. Streett. Numerical simulation of fluctuations leading to noise in a flap-edge flowfield. In *36th AIAA Aerospace Sciences Meeting and Exhibit*, Reno, NV, U.S.A., January 1998. American Institute of Aeronautics and Astronautics.
- [7] Y. Guo. Prediction of flap side edge noise. In *5th AIAA/CEAS Aeroacoustics Conference and Exhibit*, Bellevue, WA, U.S.A., May 1999. American Institute of Aeronautics and Astronautics.
- [8] Mehdi R. Khorrami, Bart A. Singer, and Ronald H. Radeztsky. Reynolds-Averaged Navier-Stokes Computations of a Flap-Side-Edge Flowfield. *AIAA Journal*, 37(1):14–22, January 1999.
- [9] Thomas F Brooks and William M. Humphreys Jr. Flap-edge aeroacoustic measurements and predictions. *Journal of Sound and Vibration*, page 44, 2003.
- [10] Yueping Guo. On noise reduction by flap side edge fences. *Journal of Sound and Vibration*, 277(1-2):369–390, October 2004.
- [11] D. Angland, X. Zhang, and N. Molin. Measurements of Flow Around a Flap Side Edge with Porous Edge Treatment. *AIAA Journal*, 47(7):1660–1671, July 2009.
- [12] Mitsuhiro Murayama, Kazuomi Yamamoto, Takehisa Takaishi, Yasushi Ito, Hiroki Ura, Yuzuru Yokokawa, Kentaro Tanaka, and Tohru Hirai. Airframe Noise Reduction of Flap Side-edge Using Vortex Generators. In *23rd AIAA/CEAS Aeroacoustics Conference*, Denver, Colorado, June 2017. American Institute of Aeronautics and Astronautics.

- [13] Torben Juul Larsen, Helge A. Madsen, and Kenneth Thomsen. Active load reduction using individual pitch, based on local blade flow measurements. *Wind Energy*, 8(1):67–80, January 2005.
- [14] C.P. van Dam, Dale E. Berg, and Scott J. Johnson. Active load control techniques for wind turbines. Technical Report SAND2008-4809, 943932, July 2008.
- [15] T.K. Barlas and G.A.M. van Kuik. Review of state of the art in smart rotor control research for wind turbines. *Progress in Aerospace Sciences*, 46(1):1–27, January 2010.
- [16] Damien Castaignet, Thanasis Barlas, Thomas Buhl, Niels K. Poulsen, Jens Jakob Wedel-Heinen, Niels A. Olesen, Christian Bak, and Taeseong Kim. Full-scale test of trailing edge flaps on a Vestas V27 wind turbine: Active load reduction and system identification: Full-scale test of trailing edge flaps on a Vestas V27 wind turbine. *Wind Energy*, 17(4):549–564, April 2014.
- [17] Alejandro Gomez Gonzalez, Peder B. Enevoldsen, Athanasios Barlas, and Helge A. Madsen. Field test of an active flap system on a full scale wind turbine. Preprint, Aerodynamics and hydrodynamics, March 2020.
- [18] Karl-Stéphane Rossignol. Development of an Empirical Prediction Model for Flap Side-Edge Noise. In *16th AIAA/CEAS Aeroacoustics Conference*, Stockholm, Sweden, June 2010. American Institute of Aeronautics and Astronautics.
- [19] Michael Pott-Pollenske and Jan Delfs. Enhanced Capabilities of the Aeroacoustic Wind Tunnel Braunschweig. In *14th AIAA/CEAS Aeroacoustics Conference*, Vancouver, British Columbia, Canada, May 2008. AIAA.
- [20] Pieter Sijtsma. CLEAN Based on Spatial Source Coherence. *International Journal of Aeroacoustics*, 6(4):357–374, December 2007.
- [21] M. Herr. Experimental Study on Noise Reduction through Trailing Edge Brushes. In Ernst Heinrich Hirschel, W. Schröder, Kozo Fujii, Werner Haase, Bram Leer, Michael A. Leschziner, Maurizio Pandolfi, Jacques Periaux, Arthur Rizzi, Bernard Roux, Hans-Josef Rath, Carsten Holze, Hans-Joachim Heinemann, Rolf Henke, and Heinz Hönlinger, editors, *New Results in Numerical and Experimental Fluid Mechanics V*, volume 92, pages 365–372. Springer Berlin Heidelberg, Berlin, Heidelberg, 2006.
- [22] Michaela Herr, Karl-Stephane Rossignol, Jan Delfs, Nicolas Lippitz, and Michael Mößner. Specification of Porous Materials for Low-Noise Trailing-Edge Applications. In *20th AIAA/CEAS Aeroacoustics Conference*, Atlanta, GA, June 2014. American Institute of Aeronautics and Astronautics.
- [23] Karl-Stephane Rossignol, Lennart Rossian, Alexandre Suryadi, Michaela Herr, Roland Ewert, and Jan Delfs. Effect of Porous Materials on the Acoustic Emissions of a Circulation-Control High-Lift Airfoil. page 4, 2020.
- [24] Michael Goody. Empirical Spectral Model of Surface Pressure Fluctuations. *AIAA Journal*, 42(9):1788–1794, September 2004.
- [25] Mark Drela. XFOIL: An Analysis and Design System for Low Reynolds Number Airfoils. In Thomas J. Mueller, editor, *Low Reynolds Number Aerodynamics*, Lecture Notes in Engineering, pages 1–12, Berlin, Heidelberg, 1989. Springer.
- [26] Nan Hu. Empirical Model of Wall Pressure Spectra in Adverse Pressure Gradients. *AIAA Journal*, 56(9):3491–3506, September 2018.

- [27] Karl-Stéphane Rossignol, Alexandre Suryadi, Michaela Herr, Johannes Schmidt, and Jörn Tytsen. Experimental Investigation of Porous Materials for Trailing-Edge Noise Reduction. *International Journal of Aeroacoustics*, 19(6-8):365–384, 2020.
- [28] Markus Lummer, Rinie A. Akkermans, Christoph Richter, Carsten Präber, and Jan Delfs. Validation of a Model for Open Rotor Noise Predictions and Calculation of Shielding Effects using a Fast BEM. In *19th AIAA/CEAS Aeroacoustics Conference*, Berlin, Germany, May 2013. American Institute of Aeronautics and Astronautics.
- [29] Nils Reiche, Roland Ewert, Markus Lummer, and Jan Delfs. Fast Multipole Boundary Element Method with Stochastic Sources for Broadband Noise Simulation. In *23rd AIAA/CEAS Aeroacoustics Conference*, Denver, Colorado, June 2017. American Institute of Aeronautics and Astronautics.
- [30] Karl-Stephane S. Rossignol. Flow Field Measurements to Characterize Flap Side-Edge Noise Generation. In *19th AIAA/CEAS Aeroacoustics Conference*, Berlin, Germany, May 2013. American Institute of Aeronautics and Astronautics.